Appl. Phys. A (2016) 122:742
DOI 10.1007/s00339-016-0266-6

Applied Physics A
Materials Science & Processing

Structural, dielectric and vibrational studies of the new mixed solid solution of thallium potassium sulfate selenate tellurate

A. Elferjani[1] · M. Abdelhedi[1] · M. Dammak[1] · A. W. Kolsi[1]

Received: 25 April 2016 / Accepted: 8 July 2016 / Published online: 16 July 2016

Abstract The new mixed compound $Tl_{1.89}K_{0.11}(SO_4)_{0.9}(SeO_4)_{0.1}Te(OH)_6$ which is crystallized in the monoclinic system with space group $P2_1/c$ was analyzed at room temperature using X-ray diffractometer data. The unit cell parameters are $a = 12.3308(7)$, $b = 7.2011(4)$, $c = 12.0298(8)$ Å, $\beta = 110.755(4)°$, $V = 998.87(11)$ Å^3 and $Z = 4$. The final refinement led to $R = 0.035$ and $Rw = 0.038$. The main feature of these atomic arrangements is the coexistence of three and different anions (SO_4^{2-}, SeO_4^{2-} and TeO_6^{6-} groups) in the unit cell, connected by hydrogen bonds (O–H···O) which make the building of the crystal. The Tl^+ and K^+ cations, occupying the same positions, are located between these polyhedral. The crystals of $Tl_{1.89}K_{0.11}(SO_4)_{0.9}(SeO_4)_{0.1}Te(OH)_6$ underwent three endothermic peaks at 377, 466 and 472 K. These transitions were detected by DSC and analyzed by dielectric measurements using the impedance and modulus spectroscopy techniques. The IR and Raman spectra recorded at room temperature in the frequency ranges (50–1200) and (400–4000) cm^{-1}, respectively, have confirmed the presence of TeO_6^{6-}, SO_4^{2-} and SeO_4^{2-} groups in the crystal.

1 Introduction

Crystals emanating from hydrogen-bonded sulfate and selenate acids exhibit many interesting physical phenomena like ferroelectricity, ferroelasticity, superionic conductivity and glassy ordering in the ferroelectronic mixture [1, 2]. Telluric acid has the property of forming stable adduct with some varieties of inorganic compounds like selenates and sulfates. Some of these compounds of the general formula $M_2XO_4Te(OH)_6$ (where M is a monovalent cation: Na^+, K^+, NH_4^+, Tl^+, Rb^+ and Cs^+, X = S, Se and P) form broad families with interesting properties, such as superprotonic conduction and ferroelectricity [3–8]. The structure of the title compound is different from those of both known $Tl_2(SO_4)_{0.61}(SeO_4)_{0.39}Te(OH)_6$ (TlSSeTe) and $K_2(SO_4)_{0.63}(SeO_4)_{0.37}Te(OH)_6$ (KSSeTe) sulfate selenate telluric alkalin. While the thallium sulfate selenate tellurate $Tl_2(SO_4)_{0.61}(SeO_4)_{0.39}Te(OH)_6$ (TlSSeTe) crystallizes in the monoclinic space group $P2_1/c$ [9], the potassium sulfate selenate tellurate $K_2(SO_4)_{0.97}(SeO_4)_{0.03}Te(OH)_6$ (KSSeTe) crystallizes in the triclinic space group P $\bar{1}$ [10]. Alkali sulfate selenate tellurate shows a structural phase transition and has interesting physical properties such as ferroelectricity and ionic protonic conduction. In order to examine the influence and the effect of cationic substitution in the sulfate selenate tellurate compounds and to confirm the presence and the importance of these physical properties, we have studied and discussed, in this work, the results of the new mixed solid solution $Tl_{1.89}K_{0.11}(SO_4)_{0.9}(SeO_4)_{0.1}Te(OH)_6$ (TlKSSeTe).

In the present paper, we report the synthesis, the structural characterization by X-ray diffraction, thermal analysis, dielectric measurements and vibrational studies of the mixed crystal (TlKSSeTe).

2 Experimental

2.1 Chemical preparation

Colorless and transparent single crystals of TlKSSeTe were grown up by slow evaporation at room temperature from a

✉ A. Elferjani
elferjani.atef@yahoo.fr

[1] Laboratory of Inorganic Chemistry, UR 11ES73, University of Sfax, B. P. 1171, 3000 Sfax, Tunisia

mixture of telluric acid H_6TeO_6, and two solutions of thallium potassium sulfate and thallium potassium selenate were prepared separately. Schematically, the reaction is as follows:

$$2\,H_2SeO_4 + Tl_2CO_3 + K_2CO_3 \rightarrow Tl_2SeO_4 + K_2SeO_4 + 2CO_2 + 2H_2O$$

$$H_6TeO_6 + x\,[y\,(Tl_2SeO_4) + (1-y)\,(K_2SeO_4)] + (1-x)\,[y(Tl_2SO_4) + (1-y)(K_2SO_4)] \rightarrow Tl_{2y}K_{2(2-2y)}(SO_4)_{(((1+y)(x-1)))}(SeO_4)_{(1-xy)}Te(OH)_6$$

Several recrystallizations were necessary to obtain single crystals suitable for the structural study. After approximately 15 days, the solutions led to colorless and transparent single crystals. The crystals obtained in this way were pure with appropriate sizes and were stable under normal conditions regarding temperature and humidity. The chemical compound formula was determined by chemical analyses and confirmed by the refinement of the crystal structure. Density was measured at room temperature by flotation in CCl_4. The density average value $D_m = 4.69$ g cm^{-3} was found to be in good agreement with the calculated one $D_{cal} = 4.79$ g cm^{-3}.

2.2 Diffraction data collection and refinement

Single-crystal X-ray diffraction intensity data were obtained on an Enraf–Nonius Kappa CCD diffractometer using Mo Kα radiation ($\lambda = 0.71073$ Å) [11]. The unit cell dimensions were measured and refined using the indexation of diffraction markings collected with a Bruker–Nonius X8-APEX2 CCD area-detector diffractometer using the APEX2 program [12].

The compound crystallizes, at room temperature, in the monoclinic system with the space group $P2_1/c$. We measured 5180 reflections, of which 2395 had an intensity of $I > 3\sigma(I)$. The structure was analyzed with the crystallographic CRYSTALS program [13]. The structural graphics were created using the DIAMOND program [14]. The final cycle of refinement leads to the final discrepancy factors $R_1 = 0.035$ and $WR_2 = 0.038$.

Other non-hydrogen atoms positions are determined from subsequent Fourier series. Furthermore, while all non-hydrogen atoms were refined anisotropically, all hydrogen atoms were geometrically fixed at the calculated positions attached to their parent atoms and treated as riding atoms. While the details of data collection, the final atomic positions and the Ueq parameters are listed in Tables 1 and 2, respectively, the anisotropic displacement parameters for the studied material are listed in Table 3, whereas the main interatomic distances (Å) and bond angles (°) for our solid solution are given in Table 4.

Table 1 Main crystallographic feature X-ray diffraction data parameters results of $Tl_{1.89}K_{0.11}(SO_4)_{0.9}(SeO_4)_{0.1}Te(OH)_6$

Formula	$Tl_{1.89}K_{0.11}(SO_4)_{0.9}(SeO_4)_{0.1}Te(OH)_6$
Formula weight (g mol^{-1})	721.14
T(K)	293
Crystal system	Monoclinic
Space group	$P2_1/c$
Unit cell dimensions	$a = 12.3308(7)$ Å
	$b = 7.2011(4)$ Å
	$c = 12.0298(8)$ Å
	$\beta = 110.755(4)°$
	$V = 998.87(11)$ Å^3
Z	4
Dx (g cm^{-3})	4.795
θ Range for data collection (°)	3.359–37.430
μ (mm^{-1})	33.964
hkl range	$-21 \le h \le 21$
	$-11 \le k \le 12$
	$20 \le l \le 20$
Data collection instrument	Kappa CCD
Wavelength (Å)	0.71073
Measured reflections	5180
Observed reflections $I > 3\sigma(I)$	2395
R indices	$R = 0.035$ and $R_w = 0.038$
Goodness-of-fit on (F^2)	1.08
Highest peak/deepest hole (eÅ^3)	$-3.04 < \Delta\rho < 3.40$
$w = 1/[\sigma^2 (Fo^2) + (0.0800P)^2 + 0P]$ where	
$P = (Fo^2 + 2Fc^2)/3$	
CCDC deposition number	1,407,320

2.3 Thermal behavior measurements

The thermo-gravimetric measurement (TG) was performed with a SETARAM TG 92 at a heating rate of 10 K min^{-1}. The masse of sample used in TG measurement was 5.8 mg, and it was heated from 350 to 550 K.

The DSC measurement was performed on 7 mg of the samples from 350 to 550 K on a NETZSCH apparatus (Model 204 Phoenix) at a heating rate of 5 K min^{-1}.

2.4 Dielectric measurements

The electrical measurements were carried out by a two-electrode configuration. The polycrystalline $Tl_{1.89}K_{0.11}(SO_4)_{0.9}(SeO_4)_{0.1}Te(OH)_6$ sample was pressed into pellets of 8 mm in diameter and 1 mm in thickness using 3t/cm^2 uniaxial pressure. As for the electrical impedances, they were measured in the frequency range from 200 Hz to

Table 2 Atomic coordinates and equivalent thermal parameters

Atoms	*x*	*y*	*z*	Uéq	Occupation
Te1	0.0000	1.0000	0.5000	0.0157	1.0000
Te2	0.5000	0.5000	0.5000	0.0154	1.0000
Tl1	0.35068(2)	1.00097(2)	0.64487(2)	0.0351	0.93093(4)
K1	0.35068(2)	1.00097(2)	0.64487(2)	0.0351	0.07093(4)
Tl2	0.14329(3)	0.53524(3)	0.39339(3)	0.0343	0.95986(2)
K2	0.14329(3)	0.53524(3)	0.39339(3)	0.0343	0.03986(2)
S1	0.24931(4)	0.50970(4)	0.74431(4)	0.0118	0.89991(4)
Se1	0.24931(4)	0.50970(4)	0.74431(4)	0.0118	0.09991(4)
O1	0.1066(6)	1.0771(8)	0.6511(6)	0.0286	1.0000
O2	0.0078(5)	0.7568(7)	0.5641(6)	0.0260	1.0000
O3	0.1292(6)	0.9392(11)	0.4552(7)	0.0361	1.0000
O4	0.3610(6)	0.3826(8)	0.3967(6)	0.0295	1.0000
O5	0.4042(7)	0.7030(11)	0.5082(10)	0.0514	1.0000
O6	0.4813(7)	0.3966(15)	0.6371(7)	0.0513	1.0000
O7	0.3533(6)	0.4866(8)	0.8559(6)	0.0323	1.0000
O8	0.2705(6)	0.4211(10)	0.6411(6)	0.0343	1.0000
O9	0.2230(6)	0.7132(8)	0.7213(7)	0.0348	1.0000
O10	0.1447(6)	0.4134(9)	0.7563(6)	0.0300	1.0000
H1	0.1004	1.1898	0.6508	0.0470	1.0000
H2	0.0437	0.6607	0.5913	0.0412	1.0000
H3	0.1456	1.0288	0.4220	0.0531	1.0000
H4	0.3830	0.2863	0.3747	0.0430	1.0000
H5	0.4317	0.7933	0.4784	0.0621	1.0000
H6	0.5327	0.2701	0.6483	0.0715	1.0000

$U_{eq} = 1/3 \sum_i \sum_j U_{ij}\, a_i \times a_j \times a_i a_j$

Table 3 Anisotropic displacement parameters of $Tl_{1.89}K_{0.11}(SO_4)_{0.9}(SeO_4)_{0.1}Te(OH)_6$ material

Atoms	U_{11}	U_{22}	U_{33}	U_{23}	U_{13}	U_{12}
Te1	0.01682(4)	0.01157(4)	0.01848(4)	0.00222(4)	0.00609(4)	0.00133(4)
Te2	0.01538(4)	0.01158(4)	0.01922(4)	−0.00004(4)	0.00621(4)	0.00195(4)
Tl1	0.03497(2)	0.03281(2)	0.03583(2)	−0.00342(2)	0.01040(2)	−0.00274(2)
K1	0.03497(2)	0.03281(2)	0.03583(2)	−0.00342(2)	0.01040(2)	−0.00274(2)
Tl2	0.03661(3)	0.03365(3)	0.03386(3)	−0.00031(3)	0.01387(3)	0.00140(3)
K2	0.03661(3)	0.03365(3)	0.03386(3)	−0.00031(3)	0.01387(3)	0.00140(3)
S1	0.01198(4)	0.00745(4)	0.01581(4)	0.00189(4)	0.00457(4)	0.00174(4)
Se1	0.01198(4)	0.00745(4)	0.01581(4)	0.00189(4)	0.00457(4)	0.00174(4)
O1	0.0335(18)	0.019(2)	0.026(2)	−0.0051(18)	0.0012(16)	0.0068(17)
O2	0.023(2)	0.0133(16)	0.039(3)	0.0093(17)	0.008(2)	0.0034(15)
O3	0.034(2)	0.046(3)	0.038(3)	0.012(2)	0.023(2)	0.011(2)
O4	0.0267(14)	0.021(2)	0.033(2)	−0.0066(19)	0.0009(17)	−0.0044(14)
O5	0.034(2)	0.035(3)	0.086(4)	−0.027(2)	0.021(3)	0.009(2)
O6	0.043(3)	0.085(4)	0.028(2)	0.010(2)	0.015(2)	−0.015(3)
O7	0.029(2)	0.023(2)	0.030(2)	0.008(2)	−0.0070(15)	0.002(2)
O8	0.037(3)	0.044(3)	0.030(2)	−0.007(2)	0.021(2)	0.001(3)
O9	0.032(3)	0.0118(13)	0.050(3)	0.009(2)	0.000(3)	0.0043(18)
O10	0.026(2)	0.029(2)	0.041(3)	−0.007(2)	0.019(2)	−0.0096(19)

Anisotropic displacement exponent takes the form: $\exp[-2\pi^2 \sum_i \sum_j U_{ij}\, h_i h_j\, a_i a_j^*]$

Table 4 Selected bond lengths (Å) and bond angles (°)

a-Thallium/potassium groups	
Tl/K(1)–O(6)(iii) = 2.808(8)	Tl/K(2)–O(4) = 2.888(7)
Tl/K(1)–O(3) = 2.906(8)	Tl/K(2)–O(1)(vii) = 2.902(7)
Tl/K(1)–O(5) = 2.917(7)	Tl/K(2)–O(8) = 2.950(6)
Tl/K(1)–O(9) = 2.940(7)	Tl/K(2)–O(2)(vi) = 2.971(6)
Tl/K(1)–O(1) = 3.085(7)	Tl/K(2)–O(3) = 3.022(8)
Tl/K(1)–O(4)(v) = 3.102(7)	Tl/K(2)–O(9)(vii) = 3.158(8)
Tl/K(1)–O(8)(iv) = 3.178(7)	Tl/K(2)–O(5) = 3.251(9)
Tl/K(1)–O(6)(iv) = 3.291(9)	Tl/K(2)–O(10)(vi) = 3.385(7)
b-Sulfate/selenate groups	
Se/S–O(7) = 1.501(6)	O(7)–Se/S–O(8) = 110.4(4)
Se/S–O(8) = 1.499(6)	O(7)–Se/S–O(9) = 109.4(4)
S/Se–O(8) = 1.499(6)	O(7)–Se/S–O(10) = 110.5(4)
Se/S–O(9) = 1.505(5)	O(8)–Se/S–O(9) = 110.6(4)
S/Se–O(9) = 1.505(5)	O(8)–Se/S–O(10) = 106.8(4)
Se/S–O(10) = 1.516(6)	O(8)–Se/S–O(10) = 110.5(4)
S/Se–O(10) = 1.516(6)	O(9)–Se/S–O(10) = 109.1(4)
	O(9)–Se/S–O(10) = 109.1(4)
c-Tellurate groups	
	O(1)(i)–Te_1–O(3)(i) = 88.5(3)
	O(1)(i)–Te_1–O(2)(i) = 87.9(3)
	O(3)(i)–Te_1–O(2)(i) = 88.6(3)
	O(1)(i)–Te_1–O(1) = 179.994
Te_1–O(1)(i) = 1.910(6)	(3)(i)–Te_1–O(1) = 91.5(3)
Te_1–O(3)(i) = 1.905(6)	O(2)(i)–Te_1–O(1)() = 92.1(3)
Te_1–O(2)(i) = 1.903(5)	O(1)(i)–Te_1–O(2) = 92.1(3)
Te_1–O(1) = 1.910(6)	O(3)(i)–Te_1–O(2) = 91.4(3)
Te_1–O(3)(i) = 1.905(6)	O(2)(i)–Te_1–O(2) = 91.4(3)
Te_1–O(2) = 1.903(5)	O(1)–Te_1–O(2) = 179.994
	O(1)–Te_1–O(2) = 87.9(3)
	O(1)(i)–Te_1–O(3) = 91.5(3)
	O(3)(i)–Te_1–O(3) = 179.994
	O(2)(i)–Te_1–O(3) = 91.4(3)
	O(1)–Te_1–O(3) = 88.5(3)
	O(2)–Te_1–O(3) = 88.6(3).
	O(4)(ii)–Te_2–O(5)(ii) = 86.8(3)
Te_2–O(4)(ii) = 1.921(6)	O(4)(ii)–Te_2–O(6)(ii) = 92.0(3)
Te_2–O(5)(ii) = 1.904(7)	O(5)(ii)–Te_2–O(6)(ii) = 89.3(5)
Te_2–O(6)(ii) = 1.904(7)	O(4)(ii)–Te_2–O(4) = 179.994
Te_2–O(4) = 1.921(6)	O(5)(ii)–Te_2–O(4) = 93.2(3)
Te_2–O(5) = 1.904(7)	O(6)(ii)–Te_2–O(4) = 88.0(3)
Te_2–O(7) = 1.896(7)	O(4)(ii)–Te_2–O(5) = 93.2(3)
	O(5)(ii)–Te_2–O(5) = 179.944
	O(6)(ii)–Te_2–O(5) = 90.7(5)
	O(4)–Te_2–O(5) = 86.8(3)
	O(4)(ii)–Te_2–O(6) = 88.0(3)
	O(5)(ii)–Te_2–O(6) = 90.7(5)
	O(6)(ii)–Te_2–O(6) = 179.994
	O(4)–Te_2–O(6) = 92.0(3)
	O(5)–Te_2–O(5) = 89.3(5)

Symmetry codes: (i) $-x, -y + 2, -z + 1$; (ii) $-x + 1, -y + 1, -z + 1$; (iii) $-x + 1, y + 1/2, -z + 3/2$; (iv) $x, y + 1, z$; (v) $x, -y + 3/2, z + 1/2$; (vi) $-x, -y + 1, -z + 1$; (vii) $x, -y + 3/2, z - 1/2$

5 MHz with the TEGAM 3550 ALF automatic bridge monitored by a microcomputer between 350 and 550 K.

By using the impedance measurements, this study undertakes the investigation of the frequency and temperature dependences of the dielectric parameters such as ε'_r and ε''_r dielectric measurements, loss tangent (tan δ), real and imaginary components of the impedance parameters (Z' and Z'') and the real and imaginary parts of the electric modulus (M' and M'').

2.5 Infrared and Raman measurements

The infrared absorption spectra of suspension of crystalline in KBr were recorded using Jasco-FT-IR-420 spectrophotometer in the frequency range of 4000–400 cm^{-1}. Besides, the Raman spectra of polycrystalline samples sealed in glass tubes were recorded on a Labrama HR 800 instrument using 632.81 nm radiations from a physics argon ion laser.

3 Results and discussion

3.1 Structural study

At room temperature, the $Tl_{1.89}K_{0.11}(SO_4)_{0.9}(SeO_4)_{0.1}Te(OH)_6$ compound is crystallized in the monoclinic system, with $P2_1/c$ space group. The unit cell parameters $a = 12.3308(7)$, $b = 7.2011(4)$, $c = 12.0298(8)$ Å, $\beta = 110.755(4)°$, $Z = 4$, $V = 998.87(11)$ $Å^3$. The asymmetric unit of $Tl_{1.89}K_{0.11}(SO_4)_{0.9}(SeO_4)_{0.1}Te(OH)_6$ shown in Fig. 1 contains Tl^+/K^+ cations, $Te(OH)_6$ octahedra and S/SeO_4 tetrahedra.

Figure 2 shows the crystal structure projection of (TlKSSeTe) on the ab plane. In this structure, three different and independent anions (TeO_6^{6-}, SO_4^{2-} and SeO_4^{2-}) in the same crystal are noted. The TlKSSeTe structure can be regarded as being built by planes of pure $Te(OH)_6$ (at $x = 0$ and $x = a/2$) octahedra, alternating with planes of pure SO_4/SeO_4 (at $x = a/4$ and $x = 3a/4$) tetrahedra. Between these kinds of polyhedra are situated the Tl^+ and K^+ cations.

The Te atom occupies two special positions in the TlKSSeTe structure. Thus, the structure shows two kinds of $Te(1)O_6$ and $Te(2)O_6$ octahedra, with Te–O values between 1896(7) and 1.921(6) Å. The O–Te–O angles vary from 86.80(3)° to 93.20(3)°.

These values are different from those observed in the previously studied compounds. Indeed, in the TlSSeTe structure, the Te–O distances vary from 1.886(10) to 1.979(11) Å with O–Te–O angles between 86.2(2)° and 93.8(2)° [9], whereas in the KSSeTe structure, the Te–O

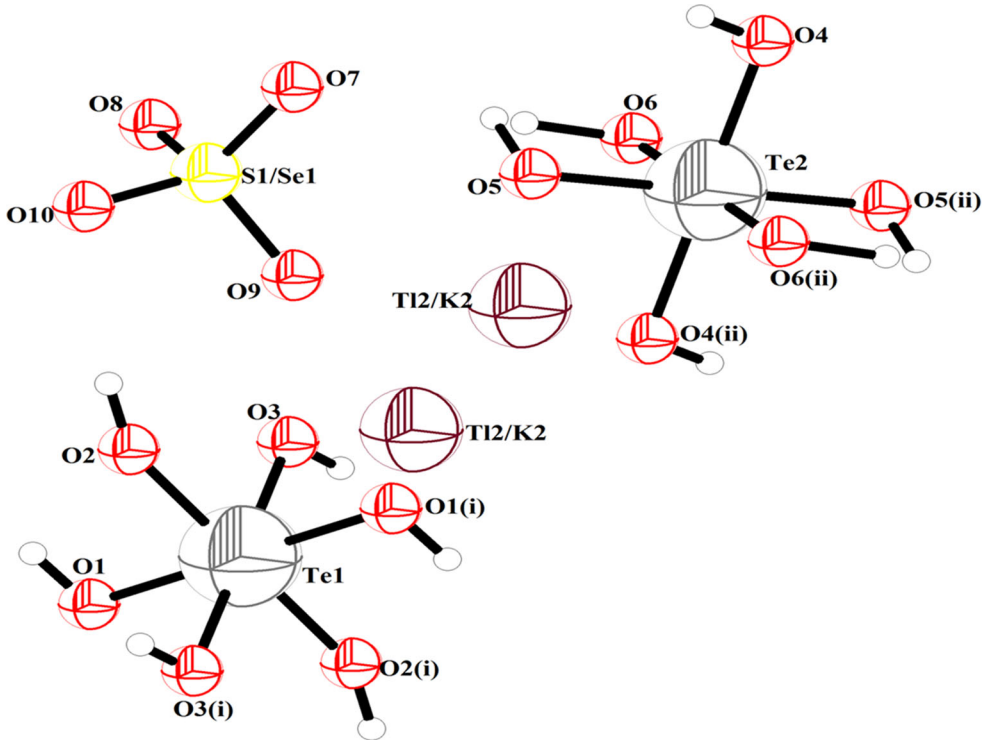

Fig. 1 Asymmetric unit with atom labels and 50 % probability displacement ellipsoids for non-H atoms of $Tl_{1.89}K_{0.11}(SO_4)_{0.9}(SeO_4)_{0.1}Te(OH)_6$

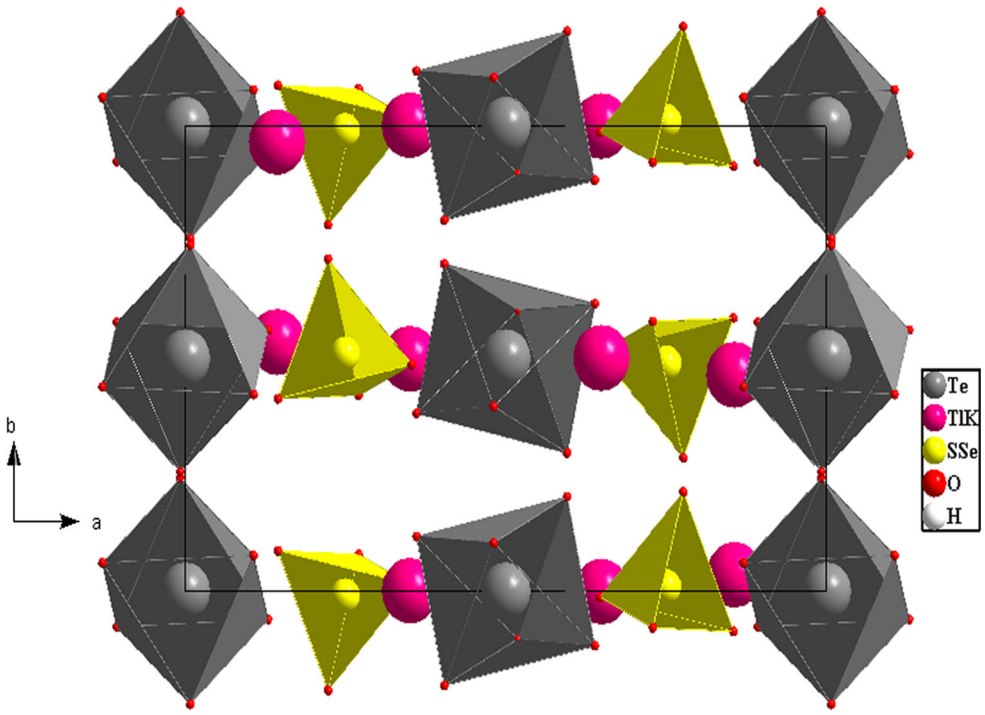

Fig. 2 Projection of crystal structure $Tl_{1.89}K_{0.11}(SO_4)_{0.9}(SeO_4)_{0.1}Te(OH)_6$ on the ab plane

Table 5 Hydrogen-bond and short-contact geometry (Å, °)

D–H···A	D–H	H···A	D···A	D–H···A
O_1–H_1···O_{10}	0.815	2.003	2.696	142.85(5)
O_3–H_3···O_{10}	0.821	2.033	2.685	136.2(6)
O_4–H_4···O_7	0.822	1.998	2.699	142.9(5)
O_5–H_5···O_7	0.868	2.147	2.817	133.7(6)

Symmetry codes: (i) $-x$, $-y + 2$, $-z + 1$; (ii) $-x + 1$, $-y + 1$, $-z + 1$; (iii) $-x + 1$, $y + 1/2$, $-z + 3/2$; (iv) x, $y + 1$, z; (v) x, $-y + 3/2$, $z + 1/2$; (vi) $-x$, $-y + 1$, $-z + 1$; (vii) x, $-y + 3/2$, $z - 1/2$

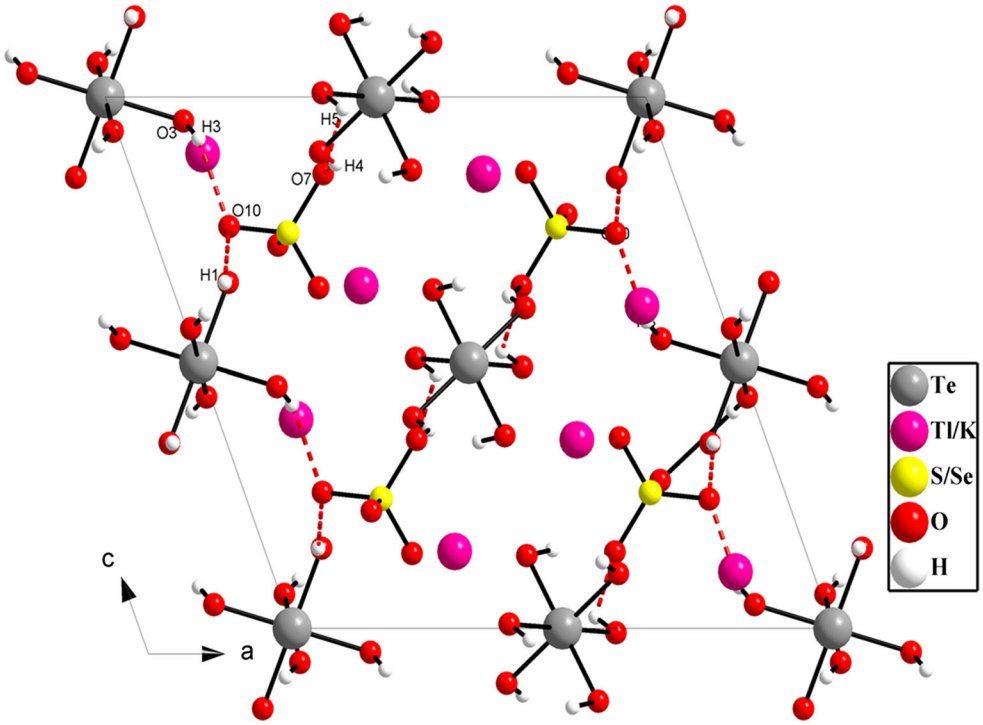

Fig. 3 Projection of the structure $Tl_{1.89}K_{0.11}(SO_4)_{0.9}(SeO_4)_{0.1}Te(OH)_6$ showing the hydrogen bonds

distances vary from 1.867(7) to 1.946(7) Å and the O–Te–O angle values are between 88.7° and 91.30° [10]. Consequently, the TeO_6 are more regular in the TlKSSeTe than in the KSSeTe compound. This phenomenon can be accredited to the partial cationic substitution.

The tetrahedral coordination of the S/Se atom is built with four oxygen atoms. In the (TlSSeTe) structure, the Se/S–O distances which vary from 1.512(11) to 1.562(9) Å form O–Se/S–O angles ranging between 107.3(4)° and 112.6(3)° [9], and in the (KSSeTe) compound, the S/Se O distances vary from 1.472(10) to 1.488(10) Å with O S/Se O angle values between 107.62(7)° and 110.45(7)° [10].

The S and Se atoms occupy the same crystallographic sites. Indeed, in the TlKSSeTe structure, the sulfur and selenium atoms occupy the same site of a statistical manner in respective proportions 90 and 10 %. In fact, the S/Se–O distances in the TlKSSeTe structure vary from 1.499(6) to 1.516(6) Å with O–S/Se–O angles ranging between 106.8(4)° and 110.6(4)°. The difference between these values and those obtained in the (TlSSeTe) and (KSSeTe) compounds [9, 10] is associated with the size of the cation radii. This phenomenon can be attributed to the partial cationic substitution. The bond lengths and angles are listed in Table 4.

The Tl^+/K^+ cations which are distributed on two sites are sandwiched between tetrahedral and octahedral planes. The Tl/K–O distances are presented in Table 4. As opposed to the (TlSSeTe) compound, in which the first Tl(1) atom is coordinated by 6 oxygen atoms and the second by seven oxygen atoms, the Tl(1)/K(1) and Tl(2)/K(2) cations in the (TlKSSeTe) structure are coordinated by eight oxygen atoms.

Therefore, the environment of Tl(1)/K(1) is made up of two oxygen atoms belonging to the tetrahedral S/SeO_4, two

oxygen atoms belonging to Te_1O_6 and four oxygen belonging to the second Te_2O_6 octahedra. The Tl(1)/K(1)–O distances are included between 2.808(8) and 3.291(9) Å. On the other hand, the Tl(2)/K(2) environment is composed of three oxygen atoms of the tetrahedral S/SeO_4, three oxygen atoms of Te_1O_6 and two oxygen atoms of Te_2O_6 octahedron. The Tl/K(1)–O distances range from 2.888(7) to 3.385(7) Å.

The (TlKSSeTe) structure stabilized by O–H···O hydrogen bonds is guaranteed by protons belonging to hydroxide groups linking octahedral and tetrahedral groups. In fact, four hydrogen atoms participate in the establishment of the hydrogen bonds (Table 5; Fig. 4). So, in the tetrahedral groups S/SeO_4, two oxygen atoms, O(7) and O(10) are linked to two hydrogen atoms (Fig. 3). Using NOVAK criterion, the O···O distances varying from 2.685 to 2.817 Å may confirm that there are two types of hydrogen bonds: strong bonds when the O···O are smaller than 2.7 Å and weak hydrogen bonds in the other case [15].

The O···H distances in this compound vary between 1.988 and 2.147 Å with O–H···O angles ranging from 133.7(6)° to 142.9(5)°. The hydrogen atoms are located geometrically in this structure.

3.2 Thermal behavior

Figure 4 shows the DSC–TG curves for the TlKSSeTe sample heated in the temperature range of 350–550 K. The thermo-gravimetric (TG) curve shows that no mass loss was detected before 400 K. Actually, in the temperature range of 400–460 K, the telluric acid $Te(OH)_6$ decomposes to disengage $2H_2O$ water molecules (calculated weight loss, 7.4 %) and gives the orthotelluric acid H_2TeO_4 [16]. The decomposition of the new compound can be described by the following reaction:

$$Tl_{1.89}K_{0.11}(SO_4)_{0.9}(SeO_4)_{0.1}Te(OH)_6 \rightarrow Tl_{1.89}K_{0.11}(SO_4)_{0.9}(SeO_4)_{0.1}H_2TeO_4 + 2H_2O$$

The DSC thermogram shows three endothermic peaks at 377, 466 and 472 K. The first and the second peaks have enthalpy values $\Delta H_1 = 4.531$ and $\Delta H_2 = 115.024$ Jg^{-1}, respectively. The superposition of TG–DSC curves, shown in Fig. 4, reveals that the endothermic peak observed at 377 K was not accompanied by a weight loss. For that, it can be related to the structural phase transition, which can favor a non-centro-symmetric phase at high temperature [17–19]. On the other hand, the second one (detected at 466 K) can be attributed to a ferroelectric–paraelectric phase transition. The same results have been reported in some previous works in the case of the studies of RbKSSeTe, RbNaSSeTe and KSeTe compounds [19–21]. The third endothermic peak observed at 472 K can be attributed to the protonic conduction phase transition due to the breaking of O–H···O hydrogen bonds which link tellurate groups to S/SeO_4 one [19–21]. On the other hand, after this thermal study, our compound preserves its solid state which confirms that the material has not reached the melting temperature [8].

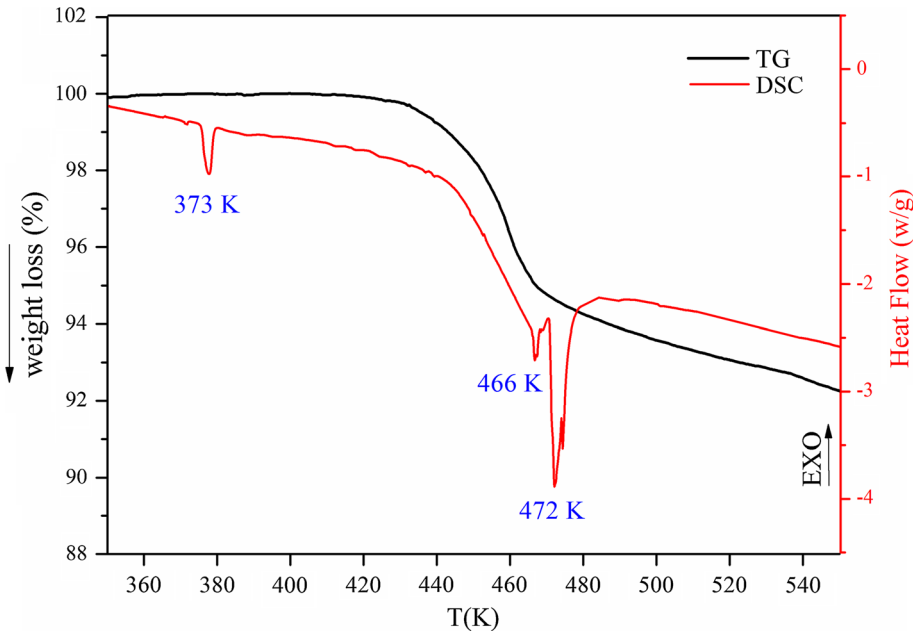

Fig. 4 Differential scanning calorimetry and thermo-gravimetric analyses of $Tl_{1.89}K_{0.11}(SO_4)_{0.9}(SeO_4)_{0.1}Te(OH)_6$

3.3 Dielectric studies

Aiming at the characterization of the phase transitions detected by DSC measurements, we have conducted a dielectric study at different temperatures in the temperature range 300–500 K.

The impedance investigation of the ionic conductors over a wide frequency range has an advantage in that it allows the identification of charge transport processes in the grains and grain boundary of compounds over a wide temperature range [22, 23]. Cole–Cole plots for $Tl_{1.89}K_{0.11}(SO_4)_{0.9}(SeO_4)_{0.1}Te(OH)_6$ at different temperatures are presented in Fig. 5a, b.

The data show a semicircle at all the temperatures. The bulk capacitance at the maximum of the semicircle can be determined using the relation: $\omega RgCg = 1$.

From these curves, the evolution curves $Z'' = f(Z')$ versus temperature show the thermal behavior of the material strength. In fact, any increase in temperature is accompanied by a decrease in resistance.

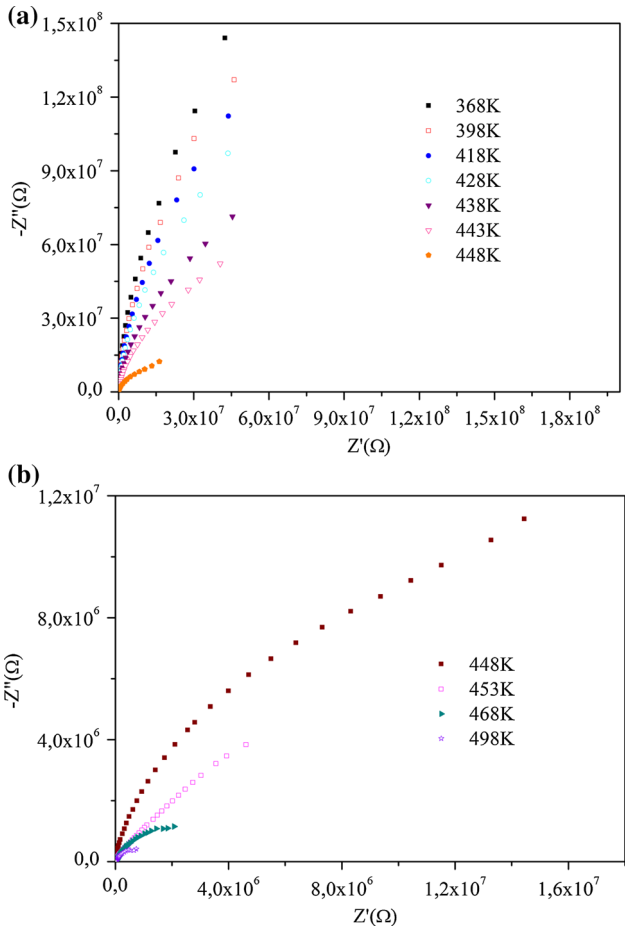

Fig. 5 Complex impedance diagrams Z'' versus Z' for $Tl_{1.89}K_{0.11}(SO_4)_{0.9}(SeO_4)_{0.1}Te(OH)_6$ over the temperature ranges. **a** 368–448 K, **b** 448–498 K

Figure 6 shows the evolution of ε'_r with temperature for different frequencies, demonstrating two anomalies on the ε'_r variation at 463 and 477 K. The first peak at 463 K, observed by DSC at about 466 K, can be attributed to the ferroelectric–paraelectric phase transition [24]. The most intense peak at 477 K characterizes the superionic–protonic phase transition [3, 25].

The important evolution of the dielectric constant with the decrease in frequency is closely related to the great contribution of the conductivity in TlKSSeTe material. Besides, the decrease in ε'_r with the increase in frequency is associated with the large and important conductivity in this material due not only to charge carriers, but also the fast mobility of the proton [26, 27]. A significant variation with the frequency is shown by the evolution of ε'_r for various

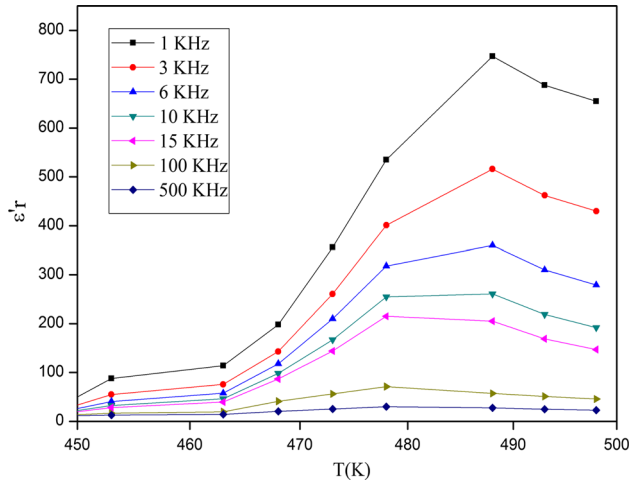

Fig. 6 Variation of ε'_r with temperature at different frequencies of $Tl_{1.89}K_{0.11}(SO_4)_{0.9}(SeO_4)_{0.1}Te(OH)_6$ compound

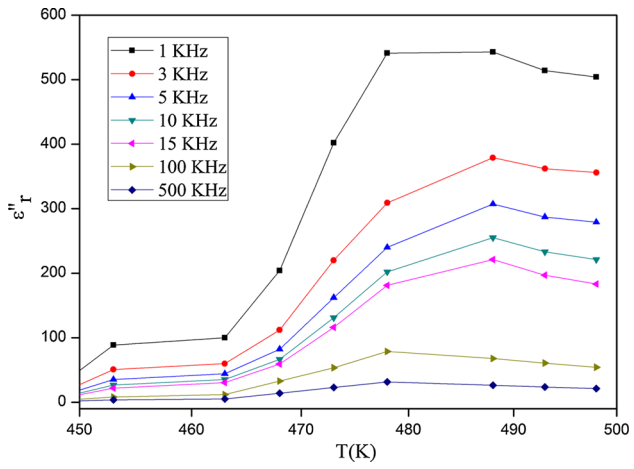

Fig. 7 Variation of ε''_r with temperature at different frequencies of $Tl_{1.89}K_{0.11}(SO_4)_{0.9}(SeO_4)_{0.1}Te(OH)_6$ compound

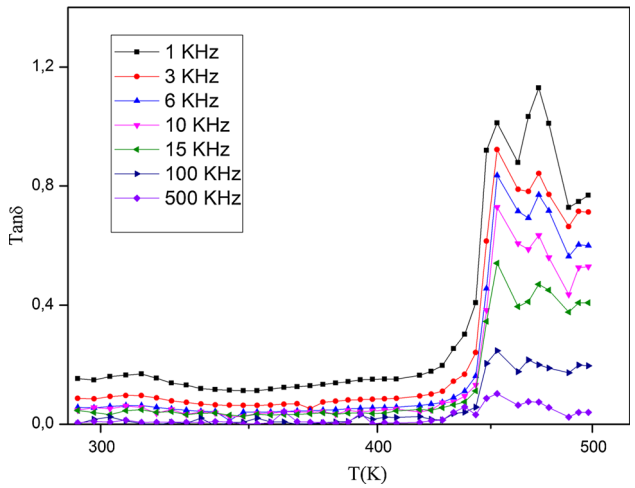

Fig. 8 Thermal evolution of the dissipation factor as a function of frequency for $Tl_{1.89}K_{0.11}(SO_4)_{0.9}(SeO_4)_{0.1}Te(OH)_6$

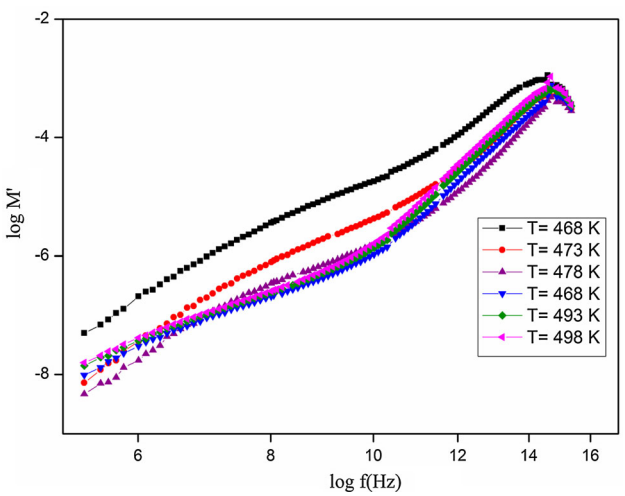

Fig. 9 Plot of log M' versus log(f) at various temperature for $Tl_{1.89}K_{0.11}(SO_4)_{0.9}(SeO_4)_{0.1}Te(OH)_6$

frequencies. This variation is due to the fact that the material presents a long-range ion diffusion. Hence, two polarization mechanisms are possible and the real part of dielectric constant can be presented as: $\varepsilon'_r = \varepsilon'_r$ (latt.) + ε'_r (carr.), where ε_r (latt.) presents the lattice response due to the permanent dipole orientation or other motions that do not involve long-range displacement of mobile charge carriers. In this contribution, we observe the changes resulting from the ferroelectric–paraelectric transition. ε'_r (latt.) presents the conductivity relaxation, or carrier response, associated with long-range migration. The second contribution is closely related to the frequency and particularly to the low frequency. This part of the permittivity characterizes the conductivity mechanisms [26, 27] (Fig. 7).

Figure 8 presents the dissipation factor (tan δ) evolution as a function of temperature. An overview of the results from these curves, we can observe two peaks at 453 and 473 K, confirmed to these phase transitions detected by DSC [3, 8, 19, 21, 28–30]. On the other hand, tan δ increases at low temperature, presenting a maximum, then decreases, presenting a minimum in the vicinity of T_c. This behavior confirms the presence of a ferroelectric–paraelectric phase transition at $T_c = 460$ K [26, 31].

The values of ferroelectric–paraelectric temperature phase transition do not change with the increase in frequency, which suggests that this compound does not present a dipolar-type relaxation in this frequency range. This phase transition is detected in the mother compound $K_2SO_4Te(OH)_6$ of our new mixed solution at 490 K.

The behavior of the dielectric permittivity ε'_r and tan δ is in agreement with a ferroelectric–paraelectric phase transition in TlKSSeTe compound at low temperature.

To shed the light on the role of Tl^+ and K^+ ions on the first transition, dielectric relaxation studies have consequently been undertaken in the complex modulus M^* formalism. Complex electric modulus plots give more importance to the elements with the smallest capacitance occurring in the dielectric system. The advantage of adopting complex electric modulus formalism is that it can discriminate against electrode polarization and grain boundary conduction mechanism [32, 33]. It is also suitable in detecting bulk phenomena properties such as apparent conductivity relaxation time. The other advantage of the electric modulus is that the electrode effect can be suppressed [34].

The complex electrical modulus (M^*) was calculated from the following equations:

$$M^* = 1/\varepsilon^* = j\omega C_0 M^* = M' + jM'' \quad (1)$$

$$M' = \omega C_0 Z'' \quad (2)$$

$$M'' = \omega C_0 Z' \quad (3)$$

where (M', Z') and (M'', Z'') are the real and imaginary parts of the modulus and impedance, respectively, $j = (-1)^{1/2}$, ω = angular frequency ($\omega = 2\pi f$) and C_0 (geometrical capacitance) = $\varepsilon_0 A/t$ (where ε_0 is the permittivity for free space, A the area of the electrode surface and t is the thickness) [34, 35]. Figures 9 and 10 reveal the plots of log M' and the normalized M''/M''_{max} imaginary part of the complex modulus of TlKSSeTe versus log f at various temperatures.

At any temperature, M' attains a constant value ($M'_\infty = 1/\varepsilon_\infty$) at high frequencies and approaches zero at low frequencies. This indicates that the electrode polarization phenomenon makes an insignificant contribution to

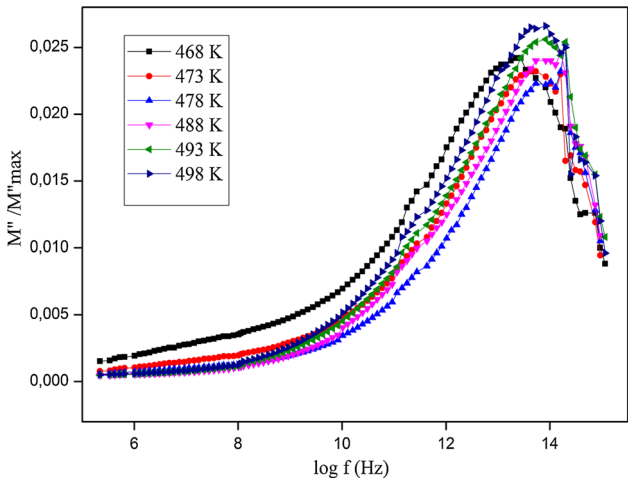

Fig. 10 Plot of normalized modulus (M''/M''_{max}) versus log(f) at various temperature for $Tl_{1.89}K_{0.11}(SO_4)_{0.9}(SeO_4)_{0.1}Te(OH)_6$

M^* and may be ignored when the electric data are analyzed in this form [36, 37].

The M''/M''_{max} spectra pertaining to a given temperature show an asymmetrical peak. Indeed, the modulus peak maximum shifts to higher frequencies with the increase in temperature.

The region of the peak maximum left is where the H^+ protons are mobile over long distances, whereas the right region is where the ions are spatially confined to their potential wells. The frequency range where the peak occurs is indicative of the transition from short-range to long-range mobility at decreasing frequency. It is defined by the condition $\omega\tau_\sigma = 1$, where τ_σ is the most probable constitution proton relaxation time [38]. This phenomenon is similar to that noted in $K_{0.84}(NH_4)_{1.16}SO_4Te(OH)_6$, which confirms that the proton transport in $Tl_{1.89}K_{0.11}(SO_4)_{0.9}(SeO_4)_{0.1}Te(OH)_6$ may be due to a hopping mechanism [39].

3.4 Vibrational study

To present further information on the crystal structure, we have examined the vibrational properties of our compound using Raman scattering and infrared absorption.

At room temperature, $Tl_{1.89}K_{0.11}(SO_4)_{0.9}(SeO_4)_{0.1}Te(OH)_6$ exhibits a monoclinic symmetry with space group $P2_1/c$. At room temperature, the Raman and IR spectroscopy were used to analyze the different observed bands of the mixed compound (TlKSSeTe).

The frequencies and assignments of the Raman and IR peaks are given in Table 6.

The study of IR and Raman spectra of this compound has been conducted in the frequency range (400–4000) and (50–1200) cm^{-1} as shown in Figs. 11 and 12, respectively. The observed frequencies are interpreted on the basis of the characteristic frequencies of the $Te(OH)_6$, SO_4 and SeO_4 groups.

Table 6 Observed Raman and IR frequencies (cm^{-1}) and band assignments for $Tl_{1.89}K_{0.11}(SO_4)_{0.9}(SeO_4)_{0.1}Te(OH)_6$ at room temperature

IR (cm^{-1})	I	Raman (cm^{-1})	I	Assignment
2976	vs	–		ν(OH) of $Te(OH)_6$
1132	s	–		υ_3 (SO_4)
984	vs	969	vs	υ_1 (SO_4)
861	m	864	w	υ_3 (SeO_4)
–		843	w	υ_2 (SeO_4)
–		827	s	υ_1 (SeO_4)
652	vs	645	vs	υ_1 (TeO_6)
–		620	s	υ_2 (TeO_6) and υ_4 (SO_4)
592	s	595	m	υ_3 (TeO_6)
–		476	w	υ_2 (SO_4) and υ_2 (SeO_4)
–		429	w	υ_4 (SeO_4)
–		419	w	υ_4 (SeO_4)
–		368	m	υ_5 (TeO_6)
–		333	m	υ_4 (TeO_6)
–		320	w	υ_2 (SeO_4)
–		221	vw	υ_6 (TeO_6)
–		172	w	υOH···O
–		108	w	T(S/SeO_4^{2-}; TeO_6^{6-})
–		72	m	T(K^+)

Relative intensities *vs* very strong, *s* strong, *m* medium, *w* weak, *vw* very weak

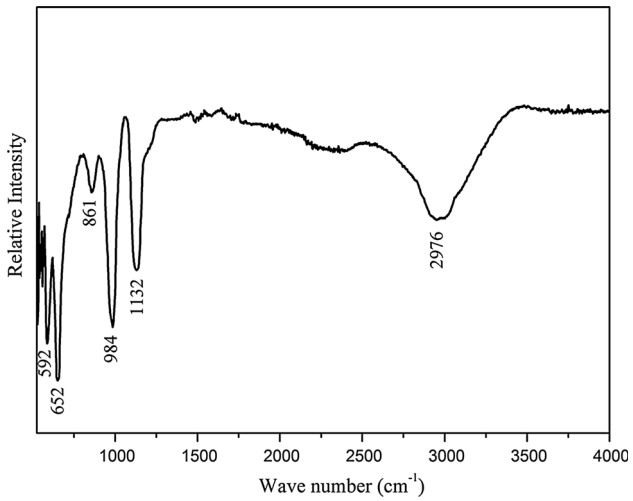

Fig. 11 IR spectrum at room temperature of $Tl_{1.89}K_{0.11}(SO_4)_{0.9}(SeO_4)_{0.1}Te(OH)_6$ compound

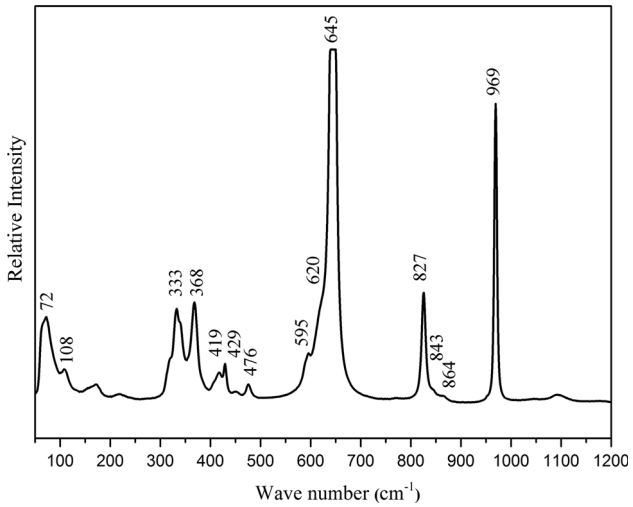

Fig. 12 Raman spectra at room temperature of $Tl_{1.89}K_{0.11}(SO_4)_{0.9}(SeO_4)_{0.1}Te(OH)_6$ compound

The stretching and bending vibrations for the compounds containing TeO_6 group normally occur in the range of 550–750 and 350–450 cm^{-1}, respectively [39–42].

The intense peak observed at 645 cm^{-1} in the Raman spectra and at 652 cm^{-1} in IR is assigned to the symmetric stretching (v_1) mode of TeO_6 [19, 20, 43–46]. Furthermore, the bands observed at 592 and 595 cm^{-1} in IR and Raman are accredited to the asymmetric stretching of v_3 (TeO_6) [45]. The peak detected at 620 cm^{-1} in the Raman spectra corresponds to v_2 (TeO_6). The band at 333 cm^{-1} is assigned to v_4 (TeO_6), and the weak peak detected at 368 cm^{-1} is attributed to v_5 (TeO_6). The band observed at 221 cm^{-1} corresponds to v_6 (TeO_6) [43].

While the intense bands observed at 964 cm^{-1} in Raman and 984 cm^{-1} in IR correspond to the symmetric stretching vibration v_1 of (SO_4), the IR line at 1132 cm^{-1} is attributed to the v_3 (SO_4). The bands observed at 476, 620 cm^{-1} in Raman spectra correspond to v_2 (SO_4) and v_4 (SO_4). The IR peak at 861 cm^{-1} range is assigned to an IR active vibration v_3 (SeO_4), and the Raman band at 827 cm^{-1} is attributed to v_1 (SeO_4) tetrahedral groups, but the line at 419 cm^{-1} is attributed to v_4 (SeO_4). The v_2 (SeO_4) vibration appears in the Raman spectra at 476 cm^{-1} [19].

The Raman peaks obtained in the low-frequency region of the spectra (<200 cm^{-1}) most likely correspond to translation modes of K^+ cations is detected at 70 cm^{-1} [39, 45, 47], and the peaks observed at 108 and 172 cm^{-1} can be associated with the vibration and translation modes of (S/SeO_4^{2-} and TeO_6^{6-}) anions [19]. As for the peak at 2976 cm^{-1} in IR, it is attributed to v (OH) of $Te(OH)_6$ [43].

4 Conclusion

The present work is devoted to the syntheses, X-ray characterization, electrical properties and vibrational study of a new mixed thallium potassium sulfate selenate tellurate, $Tl_{1.89}K_{0.11}(SO_4)_{0.9}(SeO_4)_{0.1}Te(OH)_6$. The new solid solution crystallizes in the monoclinic system ($P2_1/c$ space group) at room temperature. The structure can be regarded as being built of planes of TeO_6 octahedra and pure S/SeO_4 tetrahedra. The Tl^+/K^+ cations are intercalated between these kinds of polyhedra. The (TlKSSeTe) structure is stabilized by O–H···O hydrogen bonds assured by protons belonging to hydroxide groups which link octahedral and tetrahedral groups. The phase transitions of this compound were examined by different methods. In fact, the differential scanning calorimetry revealed three phase transitions, the first of which is detected at 377 K, which can favor the structural phase, and the second and third detected at 466 and 472 K are attributed to the ferroelectricity and the superprotonic conduction, respectively. The results of the dielectric permittivity study have confirmed the conclusion drawn from the calorimetric measurements. Some ulterior studies by impedance measurements can be carried out to affirm these transitions. The infrared and Raman spectra of the title compound, which were acquired at room temperature, confirm the presence of three different anions (TeO_6^{6-}, SO_4^{2-} and SeO_4^{2-}).

References

1. K. Jaoudi, N. Zouari, T. Mhiri, A. Daoud, M. Jannin, J. Alloy Compd. **413**, 46–53 (2006)
2. K. Jaoudi, N. Zouari, T. Mhiri, M. Giorgi, Phase Transit. **78**, 627–638 (2005)
3. H. Khemakhem, Ferroelectrics **234**, 47–59 (1999)

4. R. Zilber, A. Durif, M.T. Averbuch-Pouchot, Acta Crystallogr. B **36**, 2743–2745 (1980)
5. R. Zilber, A. Durif, M.T. Averbuch-Pouchot, Acta Crystallogr. B **37**, 650–652 (1981)
6. R. Zilber, A. Durif, M.T. Averbuch-Pouchot, Acta Crystallogr. B **38**, 1554–1556 (1982)
7. M. Dammak, H. Khemakhem, T. Mhiri, A.W. Kolsi, A. Daoud, J. Alloys Compd. **280**, 107–113 (1998)
8. M. Dammak, H. Khemakhem, T. Mhiri, J. Phys. Chem. Solids **62**, 2069–2074 (2001)
9. M. Abdelhedi, M. Dammak, A.W. Kolsi, A. Cousson, Anal. Sci. X-ray Struct. Anal. Online **24**, 93–94 (2008)
10. M. Abdelhedi, L. Ktari, M. Dammak, A. Cousson, A.W. Kolsi, Acta Crystallogr. **E63**, 153–154 (2007)
11. Nonius, in *Kappa CCD Sever Software*, ed. by B.V. Nonius (Delft, 1999)
12. APEX2 version 1. 0–8, Bruker AXS (Madison, WI, 2003)
13. D.J. Watkin, C.K. Prout, J.R. Carruthers, P.W. Betteridge, R.I. Cooper, *Crystals Issue 11* (Chemical Crystallography Laboratory, Oxford, 2001)
14. K. Brandenburg, M. Berndt, *DIAMOND Version 2.1.b*, *Crystal Impact*, *Gb R* (Bonn, 1999)
15. A. Novak, *Hydrogen Bonding in Solids*, vol. 18 (Springer, Berlin, 1974), pp. 177–216
16. J. Faby, J. Loub, L. Feltl, J. Therm. Anal. **24**, 95–100 (1982)
17. L. Ktari, M. Dammak, A.W. Kolsi, A. Cousson, J. Alloys Compd. **476**, 54–59 (2009)
18. H. Litaiem, M. Dammak, L. Ktari, S. Kammoun, T. Mhiri, Phase Transit. **77**, 929–940 (2004)
19. M. Djemel, M. Abdelhedi, L. Ktari, M. Dammak, J. Mol. Struct. **1047**, 15–21 (2013)
20. M. Abdelhedi, M. Dammak, A.W. Kolsi, J. Chem. Crystallogr. **45**, 257–265 (2015)
21. M. Dammak, H. Khemakhem, N. Zouari, A.W. Kolsi, T. Mhiri, J. Solid State Ion. **127**, 125–132 (2000)
22. A. Orilukas, A. Dindune, Z. Kanepe, J. Ronis, E. Kazakevicius, A. Kezionis, Solid State Ion. **157**, 177–181 (2003)
23. H. Kchaou, A.B. Rhaiem, K. Karoui, F. Jomni, K. Guidara, Appl. Phys. A **122**, 82–89 (2016)
24. N. Chabchoub, H. Khemakhem, M. Gargouri, J. Alloys Compd. **359**, 84–90 (2003)
25. S.G. Gauthier, J.C. Peuzin, M. Olivier, G. Rolland, Ferroelectrics **52**, 293–306 (1984)
26. H. Khemakhem, J. Ravez, A. Daoud, Ferroelectrics **188**, 41–51 (1996)
27. H. Khemakhem, R. Von der Muhll, J. Ravez, A. Daoud, Ferroelectrics **188**, 85–93 (1996)
28. M. Djemel, M. Abdelhedi, N. Zouari, M. Dammak, A.W. Kolsi, J. Solid State Chem. **196**, 267–273 (2012)
29. M. Dammak, H. Khemakhem, T. Mhiri, A.W. Kolsi, A. Daoud, J. Solid State Chem. **145**, 612–618 (1999)
30. M. Dammak, H. Litaiem, P. Gravereau, T. Mhiri, A.W. Kolsi, J. Alloys Compd. **442**, 316–319 (2007)
31. N. Zouari, M.B. Amor, T. Mhiri, A. Daoud, J.M. Réau, J. Alloys Compd. **240**, 70–75 (1996)
32. D.C. Sinclair, A.R. West, J. Appl. Phys. **66**, 3850–3856 (1989)
33. I.M. Hodge, M.D. Ingram, Q.A.R. West, J. Electroanal. Chem. Interfacial Electrochem. **74**, 125–143 (1976)
34. S. Sen, P. Pramanik, R.N.P. Choudhary, Appl. Phys. A Mater. Sci. Process. **82**, 549–557 (2006)
35. J.M. Reau, A. Simon, M. El Omari, J. Ravez, J. Eur. Ceram. Soc. **19**, 777–779 (1999)
36. F.S. Howell, R.A. Bose, P.B. Macedo, C.T. Moynihan, J. Phys. Chem. **78**, 639–648 (1974)
37. S.W. Martin, Appl. Phys. A **49**, 239–247 (1989)
38. H.K. Palet, S.W. Martin, Phys. Rev. B **45**, 10292–10300 (1992)
39. L. Ktari, M. Dammak, A. Hadrich, A. Cousson, M. Nierlich, F. Romain, T. Mhiri, J. Solid State Sci. **6**, 1393–1401 (2004)
40. R. Allman, W. Hasse, Inorg. Chem. **15**, 804–807 (1976)
41. G. Blasse, W. Hordijk, J. Solid State Chem. **15**, 395–409 (1972)
42. M. Gargouri, T. Mhiri, A. Daoud, J.M. Reau, Solid State Ion. **125**, 193–202 (1999)
43. K. Viswanathan, V.U. Nayar, G. Aruldhas, Infrared Phys. **26**, 89–91 (1986)
44. G. Sekar, K. Viswanathan, G. Aruldhas, Infrared Phys. **27**, 253–256 (1987)
45. G. Sekar, G. Aruldhas, Infrared Phys. **27**, 371–374 (1987)
46. K. Viswanathan, V.U. Nayar, G. Aruldhas, V. Ramakrishnan, J. Solid State Chem. **77**, 394–400 (1988)
47. M. Dammak, A. Hadrich, T. Mhiri, J. Alloys Compd. **428**, 8–16 (2007)